Mad dephosphorylation at the nuclear pore is essential for asymmetric stem cell division

Justin Sardi[a,1], Muhammed Burak Bener[a,1], Taylor Simao[a], Abigail E. Descoteaux[a], Boris M. Slepchenko[a,b,2], and Mayu Inaba[a,2]

[a]Department of Cell Biology, University of Connecticut Health, Farmington, CT 06030; and [b]Richard D. Berlin Center for Cell Analysis and Modeling, University of Connecticut Health, Farmington, CT 06030

Edited by Gail Mandel, Oregon Health and Science University, Portland, OR, and approved February 11, 2021 (received for review April 11, 2020)

Stem cells divide asymmetrically to generate a stem cell and a differentiating daughter cell. Yet, it remains poorly understood how a stem cell and a differentiating daughter cell can receive distinct levels of niche signal and thus acquire different cell fates (self-renewal versus differentiation), despite being adjacent to each other and thus seemingly exposed to similar levels of niche signaling. In the *Drosophila* ovary, germline stem cells (GSCs) are maintained by short range bone morphogenetic protein (BMP) signaling; the BMP ligands activate a receptor that phosphorylates the downstream molecule mothers against decapentaplegic (Mad). Phosphorylated Mad (pMad) accumulates in the GSC nucleus and activates the stem cell transcription program. Here, we demonstrate that pMad is highly concentrated in the nucleus of the GSC, while it quickly decreases in the nucleus of the differentiating daughter cell, the precystoblast (preCB), before the completion of cytokinesis. We show that a known Mad phosphatase, Dullard (Dd), is required for the asymmetric partitioning of pMad. Our mathematical modeling recapitulates the high sensitivity of the ratio of pMad levels to the Mad phosphatase activity and explains how the asymmetry arises in a shared cytoplasm. Together, these studies reveal a mechanism for breaking the symmetry of daughter cells during asymmetric stem cell division.

germline stem cells | asymmetric division | *Drosophila* | BMP signaling | Virtual Cell

The *Drosophila* female germline stem cell (GSC) is an excellent model to study niche-stem cell interaction because of its well-defined anatomy and abundant cellular markers (1). At the tip of each ovariole, two to three GSCs adhere to a cluster of niche cells, known as cap cells (CCs) (Fig. 1*A*). A bone morphogenetic protein (BMP) ligand, Decapentaplegic (Dpp), is secreted by CCs and is an essential factor for GSC maintenance (2, 3). Dpp binds to the serine–threonine kinase receptor Thickveins (Tkv) expressed on GSCs. Activated Tkv then phosphorylates Mothers against decapentaplegic (Mad) at its two C-terminal phosphorylation sites. Phosphorylated Mad (pMad) forms a heterodimer with Medea (Med), and the complex enters the nucleus and directly binds to the promoter of the differentiation factor *bag of marbles* (*bam*) to down-regulate its transcription. The down-regulation of *bam* is essential for GSC self-renewal (3–5).

It has been hypothesized that the niche signaling rapidly decreases in one of the GSC daughters, precystoblast (preCB), as it is displaced away from the CC niche. Multiple studies have defined mechanisms for fine-tuning Dpp signal strength and range (6–16). However, it is still unclear how Mad, the immediate downstream molecule of Tkv, is initially regulated during GSC division.

In this study, we demonstrate that pMad rapidly reaches different levels in the dividing GSCs after mitosis but before the completion of cytokinesis. Its level in the nuclei of future GSCs remains high, while its level in the nuclei of preCBs decreases. Upon activation of the niche signal receptor Tkv kinase, its substrate, Mad, is phosphorylated near the plasma membrane and then travels throughout the cytoplasm and enters the nucleus. After mitosis, GSC takes several hours to complete cytokinesis, and the abscission occurs during DNA synthesis (S) phase (17–19). Since preCB shares its cytoplasm with GSC during this time (20), pMad can travel freely between the cytoplasm of two daughters. How can their nuclei have different levels of pMad?

We show that the previously identified Mad phosphatase Dullard (Dd) (21) plays an essential role in the formation of the sharply different pMad levels in GSC and preCB. We demonstrate that Dd interacts with Mad at the nuclear pores, where it may directly or indirectly dephosphorylate pMad. Dd itself does not exhibit asymmetric localization in GSC and preCB, but, as our mathematical modeling indicates, the unbiased dephosphorylation by evenly distributed Dd combined with the phosphorylation of Mad biased toward the niche (due to local activation of Tkv on the niche side) is sufficient to explain the observed pMad asymmetry.

In summary, our results provide a mechanism by which a self-renewal program is confined to the stem cells during asymmetric division.

Results

GSC and preCB Establish Asymmetric pMad in Shared Cytoplasm. The niche-derived BMP signal is believed to be rapidly shut off in the preCB, a differentiating daughter, soon after it is displaced away from the niche. However, the dynamics of the signaling have never been studied.

Here, we show that pMad intensities are clearly asymmetric between GSC and preCB nuclei before the completion of cytokinesis (Fig. 1*B*). We first determined when GSCs acquire asymmetric

Significance

Stem cells often divide into two different cell types: stem cells and differentiating cells. This phenomenon, called "asymmetric cell division," is important for balancing the number of these two cell populations. Here, we demonstrate that phosphorylated Mad (pMad), the immediate downstream molecule of the niche signal, is asymmetrically partitioned within a dividing stem cell before the completion of cytokinesis. We identified a known Mad phosphatase, Dullard, as an essential factor for this process. Mathematical modeling recapitulates high sensitivity of the ratio of pMad levels to the Mad phosphatase activity and explains how the early asymmetry arises in a shared cytoplasm.

Author contributions: J.S., B.M.S., and M.I. designed research; J.S., M.B.B., T.S., A.E.D., B.M.S., and M.I. performed research; B.M.S. and M.I. contributed new reagents/analytic tools; J.S., B.M.S., and M.I. analyzed data; and T.S., B.M.S., and M.I. wrote the paper.

The authors declare no competing interest.

This article is a PNAS Direct Submission.

[1]J.S. and M.B.B. contributed equally to this work.

[2]To whom correspondence may be addressed. Email: boris@neuron.uchc.edu or inaba@uchc.edu.

This article contains supporting information online at https://www.pnas.org/lookup/suppl/doi:10.1073/pnas.2006786118/-/DCSupplemental.

Published March 22, 2021.

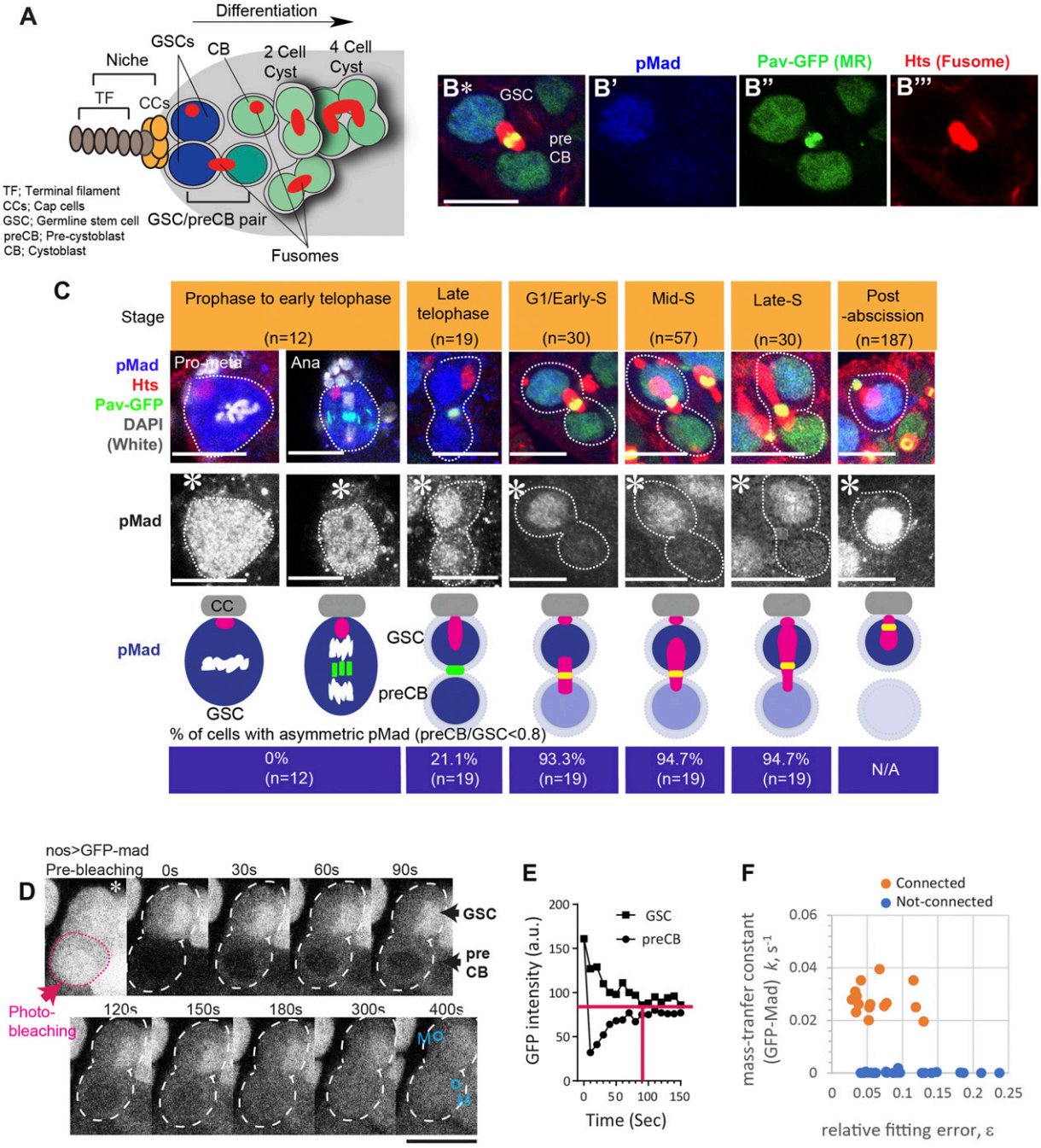

Fig. 1. GSC and preCB establish asymmetric pMad in shared cytoplasm. (*A*) Schematic of the *Drosophila* female GSC niche. (*B*) A representative confocal image of an interconnected GSC–preCB pair showing the asymmetric distribution of pMad at G1/early S stage. The fusome is a germline-specific membranous organelle marked by anti Hts (hu-li tai shao) staining (red). Pav-GFP (green) is a kinesin-like protein (MKLP1) and is known to localize at the spindle midzone, the midbody ring (MR) and in the nucleus (36). The fusome is seen running through the MR during G1/S phase. Individual channels are shown in *B'*–*B'''*. Note that Pav-GFP appears to be yellow at the MR in *B* as it overlaps with Hts. (*C*) Development of pMad asymmetry during the cell cycle. The observed number of GSCs or GSC–preCB pairs in each stage (round brackets on top) are representing the frequency of each stage. (*Upper* two rows) Representative images of anti-pMad staining of GSCs or GSC–preCB pairs in each cell cycle stage. GSCs or GSC–preCB pairs are outlined by white dotted lines. Cell cycle stages were assessed based on morphology of the fusome as previously documented (19). Specifically, the G1/S phase was subdivided into the following phases: plug/bar (G1/early S phase), stretching (mid S phase), and fusing (late S phase). The second row shows the pMad channel only. The schematics below depict an GSC or an GSC–preCB pair at each stage. Fusome is shown in red (Hts), MR is shown in green (Pav-GFP), and pMad is shown in blue. DNA (DAPI) are shown in white. Lower blue panel shows percentage of pairs with asymmetric distribution of pMad between GSC and preCB nuclei (preCB/GSC ratio <0.8, see Methods). N/A means that it is not applicable. (*D*) Representative images of GFP-Mad photobleaching experiment (Exp2 in *SI Appendix*, Table S2). Images taken before photoconversion (prebleaching) and after the indicated time points (seconds) are shown. A pink dotted line indicates the photobleached portion (entire preCB area). The blue circle (M) indicates the portion of measurements. Note that the equalization of the nuclear Mad intensity showed a delay. (*E*) Measurement of the cytoplasm intensities of GFP-Mad after photoconversion in a GSC–preCB pair shown in *D*. The pink horizontal line indicates the approximate time point in which cytoplasmic Mad reached to equalization in this pair. Numerical data for the graph are shown in Dataset S2. (*F*) Estimated mass-transfer constant by GFP-Mad redistribution after photobleaching (n = 40). Connected cells (orange dots) are characterized by faster postbleach recovery (see *SI Appendix, Supplemental Methods*). Asterisks indicate the location of CCs. (Scale bar, 10 μm.)

pMad levels, using fusome morphology as a well-established cell cycle marker (19, 22). During mitosis to early telophase, pMad was distributed uniformly throughout the cell body (Fig. 1 *C*, *Left* two panels). All tested cells in this stage had symmetric pMad (preCB/GSC was greater than 0.8, Fig. 1 *C*, *Lower*). In late telophase GSCs, pMad still exhibited similar intensities in the nuclei of most pairs of future GSCs and preCBs (Fig. 1*C*, late telophase). A total of ∼80% of cells in this stage still had a pMad ratio greater than 0.8 (Fig. 1 *C*, *Lower*). After late telophase, pMad levels rapidly became different; high in the GSC and low in the preCB. Asymmetric pMad was maintained until completion of cytokinesis (Fig. 1*C*, Gap1 (G1)/early S to late S). A total of ∼95% of cells in this stage had a pMad ratio less than 0.8 (Fig. 1 *C*, *Lower*).

A previous study indicated that GSC–preCB pairs maintain their cytoplasmic connection until the end of S phase (20), several hours after the G1/early S phase stage at which we observed pMad asymmetry. Using alpha-Tubulin (αTub)-tdEOS photoconversion assay, we confirmed that there is no diffusion barrier formed between connected cells at least until mid S phase (*SI Appendix*, Fig. S1). We next tested if the Mad protein also is freely diffusible during this phase. We expressed green fluorescent protein-tagged Mad protein (GFP-Mad) and photobleached the fluorescence in GSC or preCB and monitored redistribution of the cytoplasmic signal. GFP-Mad rapidly redistributed after photobleaching in 37.5 ± 7.6% of tested GSCs or preCBs ($n = 40$) (Fig. 1 *D* and *E* and *SI Appendix*, Table S2), similar to the percentage determined with αTub photoconversion (36.7 ± 5.1%, $n = 90$, *SI Appendix*, Fig. S1 and Table S1). These data indicate that the pMad asymmetry emerges in conditions in which pMad can freely diffuse between shared cytoplasm (*SI Appendix*, Fig. S1).

The observed cytoplasmic equilibration occurred quickly in both the αTub photoconversion and Mad photobleaching experiments. Based on curve-fitting analyses (see *SI Appendix*, *Supplemental Methods*), 90% equilibration was achieved within ∼3 min after photoconversion of αTub-tdEOS and within ∼1.5 min after photobleaching of GFP-Mad. A plot of estimated mass-transfer rates shows a cluster of pairs with faster recovery of GFP-Mad in a visibly separate single group (orange dots in Fig. 1*F*, characterized by $k > 0.01$ s^{-1}, see *SI Appendix*, *Supplemental Methods*) from unconnected pairs (blue dots in Fig. 1*F*), further indicating that no diffusion delay occurs for Mad protein during the estimated phases. Moreover, we did not detect any immobilized fraction of Mad in the GFP-Mad photobleaching experiment, suggesting that all Mad is diffusible (Fig. 1*D* and Movie S1).

Asymmetric pMad distribution, despite rapid equilibration of the cytoplasmic Mad throughout the G1/S phase, prompted us to investigate the cellular mechanism that establishes pMad asymmetry. Hereafter, we refer the asymmetric pMad distribution between GSC and preCB nuclei during G1/S phase to as "G1/S pMad asymmetry."

Dd Is Required for the Establishment of G1/S pMad Asymmetry. We found a putative Mad phosphatase, Dd, as a gene required for the establishment of G1/S pMad asymmetry. The previously reported *Dd* hypomorphic allele, ddd^{p}, which has a P element inserted into the 5′-untranslated region of *Dd* gene (23), as well as a germline-specific *Dd* knock down (*nosGal4 > Dd RNAi*, see Methods) both showed compromised G1/S pMad asymmetry. During mitosis, pMad distribution was uniformly observed *Dd* mutant GSCs similar to control GSCs (Fig. 2 *A*, *Left* three time points). In control GSC–preCB pairs, the nuclear pMad distribution became asymmetric shortly after late telophase (Fig. 1*C*). However, without Dd, the two nuclei continued to exhibit similar levels of pMad throughout the G1/S phase (Fig. 2 *A* and *B*). In the control, the pMad ratio (preCB/GSC) in G1/early S phase was significantly lower than that in late telophase ($P < 0.0001$) (Fig. 2*C*). No significant difference in the pMad ratio between late telophase and G1/early S phase was observed ($P > 0.05$ both in *Dd* mutant and RNA interference [RNAi]), and the high pMad ratio (preCB/GSC) lasted for the entire G1/S phase (Fig. 2*C*). These data suggested that Dd is required for the establishment of G1/S pMad asymmetry.

Roles of Other Factors in G1/S pMad Asymmetry. Surprisingly, G1/S pMad asymmetry was observed even when the constitutive active (CA) form of Tkv was overexpressed (Fig. 2*D*, *nosGal4 > TkvCA*). In such ovaries, the absolute pMad level in GSC was higher than that in control GSC, indicating that the kinase activity was indeed increased (Fig. 2*E*). However, the ratio of nuclear pMad in the interconnected GSC–preCB pairs remained the same as in the control pairs (Fig. 2*F*), indicating that the increased kinase activity does not impact the G1/S pMad asymmetry. This finding confirms the prediction of the mathematical model to be described in a subsequent section. We could not experimentally test the "decreased" kinase activity as GSCs cannot be maintained in the *tkv* mutant ovary (2).

In addition, neither the knock down of genes regulating the proteasome function nor overexpression of degradation-defective Mad (*nosGal4 > Mad-MGM*) (24) altered the G1/S pMad ratio (Fig. 2 *G*, *H*, and *J*), suggesting that the rate of Mad degradation also does not influence the G1/S pMad asymmetry.

The Fused (Fu)/Smurf axis was previously documented to be required for ensuring an asymmetric cell fate of GSC and preCB (13). Fu is a serine–threonine kinase that phosphorylates Tkv and promotes its ubiquitination by E3 ligase Smurf and subsequent degradation. On the other hand, pMad promotes the degradation of Fu; therefore, Fu is concentrated only in the preCB. These mechanisms initiate a feedback loop to enhance the gradient of BMP response downstream of the niche signal (6). To understand the relationship between the roles Dd and Fu play in BMP signal regulation, we compared the phenotype of the *Dd* mutant (ddd^{p}/ddd^{p}) with that of an *fu* mutant using the previously reported *fu* mutant allele (*fuA*) (13). In *fuA* ovaries, GSC–preCB pairs maintained pMad asymmetry in the G1/S phase (Fig. 2 *G*, *I*, and *J*), indicating that the Fu-mediated feedback loop does not have an impact on GSC–preCB pairs before the completion of cytokinesis. However, Fu mutant germ cells retained intermediate levels of pMad after exit from niche (*SI Appendix*, Fig. S2 *A–C*), suggesting that Fu likely functions at later time points, to further ensure the differentiation of preCB.

Taken together, we concluded that the Dd-mediated pMad dephosphorylation is essential for establishment of pMad asymmetry during G1/S phase. The rate of kinase activity, the rate of Mad degradation, and the Fu/Smurf axis all do not influence pMad asymmetry in this time period.

Both Dd Protein Level and Dd–Mad Interaction Do Not Show Asymmetry. To understand how Dd regulates G1/S pMad asymmetry, we first examined the localization of Dd by anti-Dd antibody staining (Fig. 3*A*). Dd has been shown to localize to the nuclear envelope (21, 23). Consistently, we observed Dd along the nuclear envelope (illuminated by LaminDM0) and perinuclear region (Fig. 3*B*). The Dd was not detectable in the *Dd* mutant (ddd^{p}/ddd^{p}) germaria (Fig. 3*C*), indicating that this Dd antibody specifically recognizes Dd protein. A similar localization pattern was observed with a *Dd* transgene expressed in the germline (*nosGal4 > Dd-VNm9*, N-terminal half of Venus [VNm9] fused to *Dd*, visualized by an anti-GFP antibody staining) (Fig. 3*D*). Notably, although our data indicate that Dd contributes to establishing unequal levels of pMad between GSC and preCB, Dd protein levels were the same in both cells (Fig. 3*A*). The Dd intensity ratio comparing preCB and GSC was 0.97 ± 0.21 ($n = 8$).

We next wondered whether the rate of Dd and Mad interaction may differ between GSC and preCB, thus creating the observed pMad gradient. To visualize the interaction of Dd and Mad, we employed a bimolecular fluorescence complementation (BiFC) assay (25). When Dd was fused to VNm9 (26), and Mad was fused

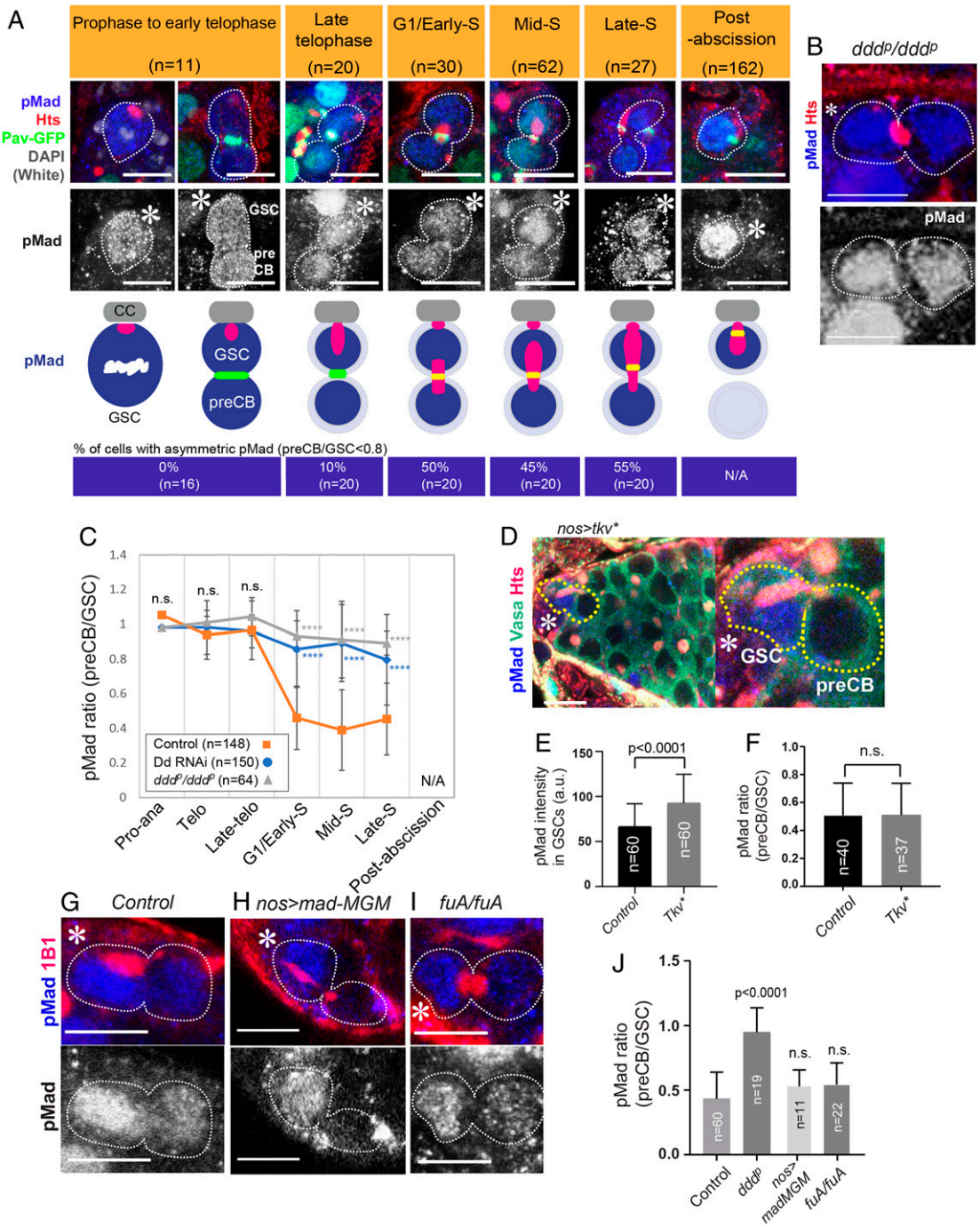

Fig. 2. Dd is required for the establishment of G1/S pMad asymmetry. (*A*) The observed number of GSCs or GSC–preCB pairs in each stage (round brackets on top). (*Upper* two rows) The representative images of anti-pMad staining of GSCs or GSC–preCB pairs in each cell cycle stage in a *Dd* RNAi ovary (*nosGal4* > *Dd RNAi*). GSCs or GSC–preCB pairs are outlined by white dotted lines. Cell cycle stages were assessed based on morphology of the fusome (see legend for Fig. 1*C*). The second row shows the pMad channel only. The schematic below depicts an GSC or an GSC–preCB pair at each stage. The lower blue panel shows the percentage of pairs with asymmetric distribution of pMad between GSC and preCB nuclei (preCB/GSC ratio <0.8, see Methods). Fusome is shown in red (Hts), MR is shown in green (Pav-GFP), and pMad is shown in blue. DNA (DAPI, white) staining is shown for a proanaphase image. (*B*) A representative image of anti-pMad staining of a G1/S phase GSC–preCB pair in an ovary from the *Dd* hypomorphic mutant (ddd^{P}/ddd^{P}). Fusome is shown in red (Hts) and pMad is shown in blue. A white dotted line encircles an GSC–preCB pair. (*C*) Average ratio of nuclear pMad intensities of GSC–preCB pair (preCB/GSC) in each cell cycle stage from indicated genotypes (see Methods for more details). N/A means it is not applicable. (*D*) Representative images of a germarium expressing TkvCA under the germline-specific driver (*nosGal4* > *tkvCA*). An GSC–preCB pair in G1/S phase is encircled by yellow dotted lines. Hts is shown in red (fusome), Vasa is shown in green (germ cell), and pMad is shown in blue. (*E*) Quantification of pMad intensity in the nucleus of a G1/S phase GSC from indicated genotypes. (*F*) The ratio of nuclear pMad intensities of a G1/S phase GSC–preCB pair (preCB/GSC) from indicated genotypes. (*G–J*) Representative images of GSC–preCB pairs in G1/S phase from indicated genotypes. Fusome is shown in red (Hts) and pMad is shown in blue. GSCs and preCBs are outlined by white dotted lines. (*J*) The ratio of nuclear pMad intensities of a G1/S phase GSC–preCB pair (preCB/GSC) from indicated genotypes. Asterisks indicate the location of CCs. (Scale bar, 10 μm.) *P* values (adjusted *P* values from Dunnett's multiple comparisons test for *C* and *J*, from Student's *t* test for *E* and *F*) are provided as ****$P < 0.0001$; n.s., nonsignificant ($P \geq 0.05$).

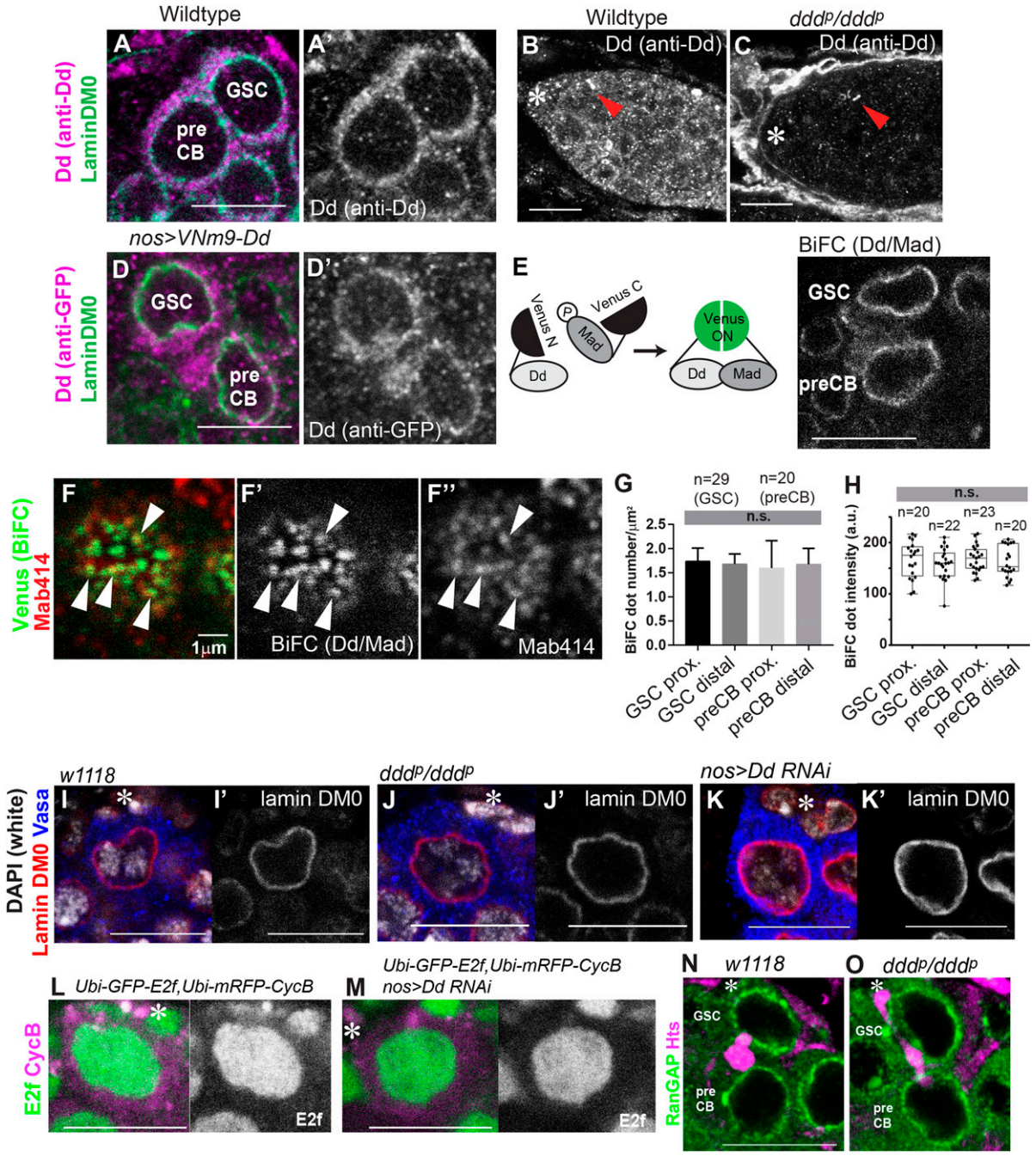

Fig. 3. Dd protein level and Dd–Mad interaction both do not show asymmetry. (*A*–*C*) Representative images of germaria costained with Dd (anti-Dd, magenta) and a nuclear envelope marker, Lamin DM0 (green) from a wild-type (w1118, *A* and *B*) or a *Dd* mutant (ddd^{P}/ddd^{P}, *C*) ovary. Note that the Dd antibody also stained contractile rings in the germarium (a red arrowhead in *B*), this was likely a nonspecific signal as it also remained in the *Dd* mutant germarium (a red arrowhead in *C*). (*D*) A representative image of anti-GFP staining (magenta) of an GSC–preCB pair expressing VNm9-tagged Dd under the nosGal4 driver (*nosGal4* > *Dd-VNm9*). Lamin DM0 is shown in green. (*E*, *Left*) Schematic of Dd-Mad BiFC design. The N terminus half and C terminus half of Venus were fused to the C terminus of Dd and the N terminus of Mad, respectively. When these constructs are expressed together, Venus is reconstituted upon Dd–Mad interaction and emits fluorescence. (*Right*) A representative image of an GSC–preCB pair expressing both Dd-VNm9 and VC-Mad (*nosGal4* > *Dd-VNm9*, *VC-mad*). The Dd–Mad BiFC signal was observed along the nuclear envelope. (*F*) The Dd–Mad BiFC signal was observed as spots on the nuclear membrane. Arrowheads show colocalization of the BiFC signal and the pan-nuclear pore marker, Mab414, staining. BiFC is shown in green and Mab414 is shown in red. (*G*) Quantification of BiFC dots in different portions of GSC and preCB nuclei. The proximal half of the nuclear envelope, close to CCs (Prox) and the distal half of the nuclear envelope (Distal). The 2×2 μm nuclear surface regions (from the indicated number of GSCs and preCBs) from two independent experiments were scored for each data point. (*H*) Quantification of BiFC dot intensity in different portions of GSC and preCB nuclei. The indicated number of dots were scored from five cells for each region. For *G* and *H*, the adjusted *P* value was calculated from Dunnett's multiple comparisons test; n.s.: nonsignificant ($P \geq 0.05$). (*I*–*K*) Representative images of GSCs with anti-Lamin DM0 (red) and anti-Vasa staining (blue) from indicated genotypes. DAPI is shown in white. *Right* panels show the Lamin DM0 channel. (*L* and *M*) Representative images of an GSC expressing GFP–E2f 1 to 230 (green), mRFP–CycB (magenta) under the ubiquitin promoter (*Ubi-GFP-E2f* 1 to 230, *Ubi-mRFP-CycB)* from indicated genotypes. *Right* panels show the E2f (green) channel only. (*N* and *O*) Representative images of anti-RanGAP staining (green) of an GSC–preCB pair from indicated genotypes. Hts is shown in magenta (fusome). All GSC–preCB pairs shown are in G1/S phase (*B*, *D*, *E*, *N*, and *O*). Asterisks indicate the location of CCs. (Scale bar, 10 μm unless otherwise indicated.)

with the C-terminal half of Venus (VC) (Fig. 3*E*, *nosGal4 > Dd-VNm9*, *VC-mad*), a strong BiFC signal was observed as a punctate pattern along the nuclear envelope (Fig. 3 *E* and *F*). This BiFC signal colocalized with nuclear pore marker Mab414 (Fig. 3*F*), indicating that Mad interacts with Dd at the nuclear pore. The BiFC signal was not visible if only one of the constructs was expressed (*SI Appendix*, Fig. S3 *A–C*). In addition, we observed a distinct localization pattern when Medea-VNm9 instead of Dd-VNm9 was expressed with VC-Mad (*nosGal4 > medea-VNm9, VC-mad*, BiFC signal was observed in nucleus instead of nuclear envelope, *SI Appendix*, Fig. S3*D*), indicating that the Dd-VNm9/VC-Mad BiFC signal was specific for the Dd–Mad interaction at the nuclear pore. Throughout the GSC and preCB nuclei, no difference in number and intensity of BiFC puncta (Fig. 3 *G* and *H*) was observed, indicating that Dd–Mad interaction occurs equally in GSC and preCB.

Although Dd was reported to be required for nuclear envelope integrity in yeast (27), we did not observe aberrant nuclear envelope morphology in GSCs or preCBs in the absence of Dd (Fig. 3 *I–K*). Furthermore, the nuclear localization of GFP-tagged E2f protein (22, 28) did not show a detectable change of its nuclear distribution in *Dd* mutant GSCs (Fig. 3 *L* and *M*), indicating that nuclear envelope was intact in *Dd* mutant GSCs. Dd has also been reported to affect localization of RanGAP protein, a major regulator of nuclear import/export (23). We did not observe aberrant RanGAP localization in the *Dd* mutant compared with the control (Fig. 3*N*). These data suggest that the loss of pMad asymmetry in the *Dd* mutant is not because of any change in nuclear envelope integrity or rate of nuclear export/import but rather because of the lack of Dd-mediated dephosphorylation of Mad.

In summary, our results indicate that Dd interacts with Mad at the nuclear pore for dephosphorylation. Neither the Dd protein level nor Dd–Mad interaction between GSCs and preCBs was asymmetric (Fig. 3 *D*, *G*, and *H*), indicating that pMad asymmetry does not originate from an asymmetric localization/function of Dd. How then does Dd contribute to establishing pMad asymmetry?

Modeling Suggests That pMad Asymmetry Emerges because of the Interplay of Phosphatase Activity and pMad Diffusion. The localization of active kinase (Dpp-bound Tkv) in the GSC–preCB pair is asymmetric. As reported (9, 11, 29–31), the Dpp ligand is highly concentrated and stabilized on the surface of CCs, and a recent study demonstrated that GSCs project cellular protrusions into CCs to access a reservoir of Dpp (29). Because, on the other hand, somatic escort cells surrounding GSCs express Tkv receptor to absorb any free Dpp (30), the activation of Tkv receptor is constrained to the side of GSC near the niche. However, the asymmetric localization of activated receptors alone is insufficient for establishing a sharply asymmetric pMad distribution: As we showed in the previous sections, pMad dephosphorylation is necessary for the asymmetry.

To understand how Dd, that is evenly distributed between the nuclei of the GSC and preCB, contributes to establishing the pMad asymmetry, we constructed a mathematical model involving essential processes that may affect pMad accumulation in the nuclei of a dividing stem cell (Fig. 4 *A–C*). The model includes the following: 1) the phosphorylation of Mad by activated kinase receptors residing on the plasma membrane at the pole of GSC; 2) the diffusion of Mad and pMad throughout the shared cytoplasm; 3) the shuttling of pMad and Mad between the cytosol and nuclei via nuclear pores; 4) the binding of pMad in the nuclei of GSC and preCB to the nuclear matrix and DNA; 5) the dephosphorylation of free pMad by phosphatases in the inner leaflet of the nuclear envelope; and 6) the diffusion of free pMad and Mad in the nuclei (Fig. 4*C*). Except for the phosphorylation event occurring only at the pole of GSC, identical parameters were used to characterize the same processes in GSC and preCB (Fig. 4*C*). The model was solved in a three-dimensional (3D) geometry mimicking a shape of a cell undergoing cytokinesis (Fig. 4 *A* and *B*; see Methods). The kinase (activated Tkv receptor) is assumed to be concentrated within a "cap" shown in red in Fig. 4*B*.

We solved the model with parameters listed in Table 1. The parameter values were constrained by the data of Figs. 1 *D* and *E* and 2*C* and by experimentally measured GSC nucleus/cytoplasm ratios of pMad concentrations and the GSC/preCB nuclear ratios of total Mad (both phosphorylated and unphosphorylated).

Consistent with the experimental data (Fig. 2*C*), the simulations run with Dd evenly partitioned between the nuclei yielded the preCB/GSC nuclear ratio of pMad of ∼0.5 (Fig. 4*D*). Notably, the pMad asymmetry emerged only in the simulations with sufficiently high phosphatase activity. In the limit of low phosphatase activity, the preCB/GSC nuclear ratios of pMad approached unity. In particular, a 10-fold decrease of phosphatase activity yielded a pMad nuclear ratio of ∼0.9 (Fig. 4*E*), consistent with the *Dd* mutant experiments (Fig. 2*C*). Thus, the model was able to reproduce the experimental data.

We next analyzed the model to determine factors that had the most impact on the pMad nucl1/nucl2 ratio (here and below, "nucl1" and "nucl2" denote the GSC and preCB nuclei, respectively). Counterintuitively, those factors did not include kinase activity, see Fig. 4*F* showing sensitivities of the steady-state pMad ratio to fivefold changes (increases and decreases) of standard parameters. The experiments with constitutively active Tkv receptors confirmed the model prediction: The pMad nucl1/nucl2 ratios measured in these cells were indeed similar to those in the control experiments (Fig. 2 *E* and *F*).

The sensitivity analysis distinguished pMad diffusivity as the only other parameter whose effect on the pMad asymmetry was comparable to that of phosphatase activity. Thus, the pMad nucl1/nucl2 ratio is largely determined by the interplay of phosphatase activity and pMad diffusion. As we argue in the next section, to be sufficient for establishing sharp pMad asymmetry, the phosphatase activity must overcome dissipation effects of pMad diffusion.

The Underlying Mechanism: Origins of pMad Gradients and Their Steepness. The nuclear pMad, albeit enhanced by unequal permeabilities of the nuclear envelope to inward/outward pMad fluxes and due to binding to the nuclear matrix, is in a dynamic equilibrium with the neighboring cytosolic pMad, making the nucl1/nucl2 ratio an amplified reflection of steady-state gradients of pMad in the cytosol. The gradients of cytosolic pMad, in turn, originate from the distinct localizations of the Tkv receptors and Dd molecules.

Further insights into sensitivities of the 3D model can be gained from a stripped-down one-dimensional (1D) model of cytosolic pMad, which has a simple analytical solution. In this model, pMad is produced by a kinase at a "left" cell boundary and diffuses into the cell interior, where it is dephosphorylated by an evenly distributed phosphatase (Fig. 4*G*) [similar "source-diffusion–degradation" models are often used to describe effects of concentration gradients in morphogenesis (32) and cell signaling (33)]. Ignoring for simplicity effects of the "right" boundary (i.e., assuming that the cell length is much greater than the characteristic gradient length λ defined below), the pMad concentration as a function of a local coordinate x is described by a single exponential, $[pMad](x) = [pMad](0)\exp(-x/\lambda)$, exemplified by the black curve in Fig. 4*G*. The pre-exponential factor $[pMad](0)$ is the pMad concentration at the left end, which depends on kinase activity (k_1).

The length parameter λ, characterizing the steepness of pMad gradient, is determined exclusively by the pMad diffusivity (D) and phosphatase activity constant (k_2): $\lambda = \sqrt{D/k_2}$ (note that because the phosphatase in this model is distributed throughout the cell, the units of k_2 are s^{-1}). Using the solution of this model,

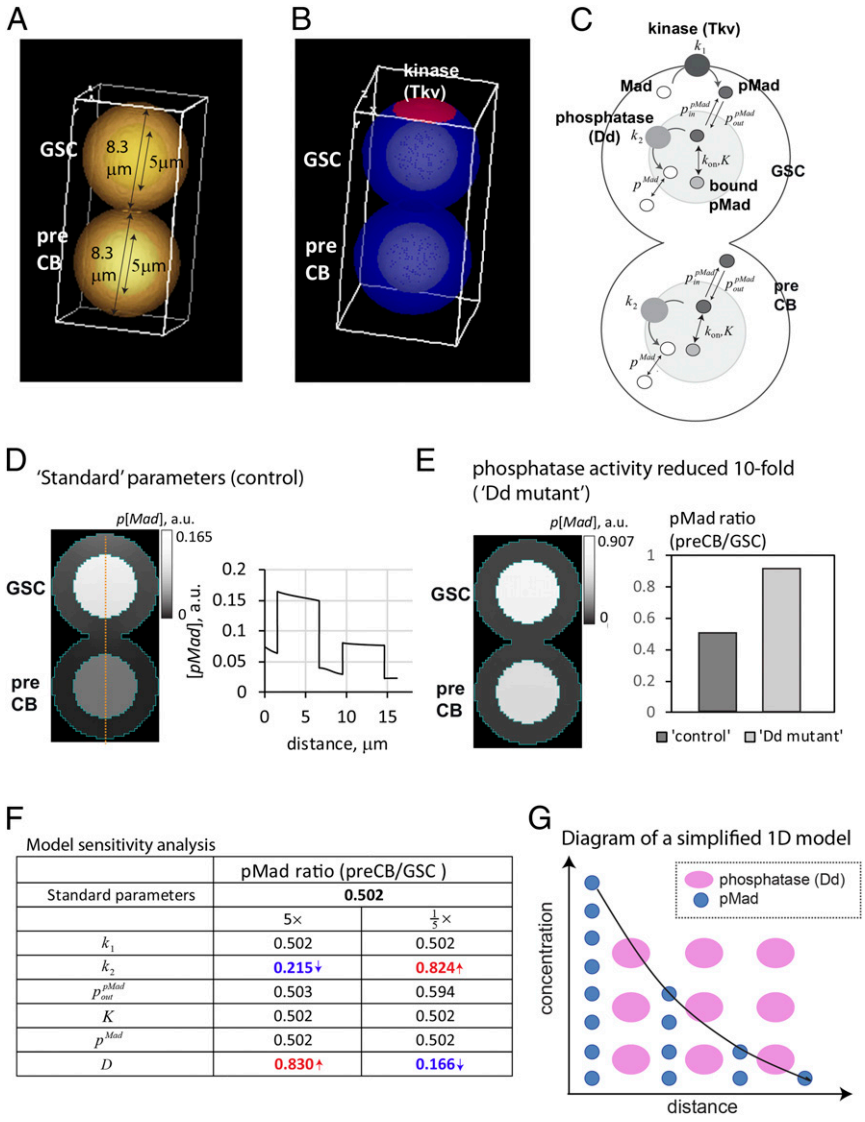

	pMad ratio (preCB/GSC)	
Standard parameters	**0.502**	
	5×	$\frac{1}{5}$×
k_1	0.502	0.502
k_2	**0.215**↓	**0.824**↑
p_{out}^{pMad}	0.503	0.594
K	0.502	0.502
p^{Mad}	0.502	0.502
D	**0.830**↑	**0.166**↓

Fig. 4. The mathematical model shows that pMad asymmetry is determined by the interplay of phosphatase activity and pMad diffusion. (*A*) Model geometry. (*B*) Simulated localization of the kinase (shown in red). (*C*) Reactions and fluxes essential for pMad partitioning between daughter cells. (*D*) (*Left*) The pMad distribution, obtained by solving 3D model with "standard" parameters (Table 1), recapitulates wild-type experimental results. (*Right*) The line scan of [p*Mad*] along the vertical axis (dashed line in the *Left* panel). (*E*, *Left*) The 10-fold reduction of phosphatase activity in 3D model yields pMad distribution consistent with *Dd*-mutant data. (*Right*) The simulated pMad preCB/GSC ratio for *Dd* mutant and control conditions. (*F*) Sensitivities of the pMad nuclear ratio to fivefold increases and decreases of model parameters indicate strong dependence of pMad asymmetry on phosphatase activity and pMad diffusivity (for parameter definitions and values, see Table 1). (*G*) Diagram of a simplified 1D model, in which pMad (blue circles) is produced at a left boundary, diffuses inside the cell, and gets dephosphorylated by an evenly distributed phosphatase (pink ovals).

a ratio of $[pMad](x)$ at two points separated by a given distance d is $\exp(d/\lambda)$. Therefore, this ratio is sensitive only to k_2 and D (not k_1): dephosphorylation of pMad makes pMad gradients steeper, whereas pMad diffusion levels them out.

In the more realistic 3D model, the properties of the pMad distribution in the cytosol are conferred on the pMad nucl1/nucl2 ratios due to the abovementioned dynamic equilibrium between the cytosolic pMad in the vicinity of the nuclei and the nuclear pMad. Thus, the 1D model, notwithstanding the simplifications, correctly captures salient properties of the 3D model and provides insight into mechanisms behind asymmetric partitioning of pMad (we note in this regard that the cytosolic portions of the line scan in Fig. 4*D* are, for the most part, well approximated by a single exponential, *SI Appendix*, Fig. S4).

The pMad ratio becomes large if $\lambda < d$ or, in other words, if the time $1/k_2$ required for dephosphorylating a pMad molecule is shorter than the time d^2/D that the pMad molecule takes to diffuse a distance separating the two nuclei. Because the dephosphorylation in the realistic 3D model occurs on the inner leaf of the envelope, the effective dephosphorylation time includes also the time of crossing the envelope, which depends on the envelope permeabilities. This explains some sensitivity of the pMad ratio to the permeability of nuclear pores to pMad import/export from a nucleus (Fig. 4*F*).

In summary, the model reproduces the experimentally observed asymmetric accumulation of pMad during *Drosophila* female GSC division. The model also shows that this is a robust phenomenon originating from separation of kinases and phosphatases, which sets up gradients of cytosolic pMad. The steepness of these gradients and, therefore, the sharpness of the nucl1/nucl2 ratio is determined exclusively by the effective dephosphorylation rate and pMad diffusivity in the cytoplasm.

Table 1. "Standard'" parameter set

Parameter	Notation	Value	Units
Kinase activity	k_1	30/602 = 0.0498	μm/s
Phosphatase activity	k_2	45/602 = 0.0747	μm/s
pMad nuclear export coefficient	p_{out}^{pMad}	0.48	μm/s
pMad nuclear import coefficient	p_{in}^{pMad}	1.792 $\cdot p_{out}^{pMad}$	μm/s
Rate constant of pMad binding to nuclear matrix	k_{on}	1	s^{-1}
Equilibrium constant for pMad binding to nuclear matrix	K	1	Dimensionless
Mad nuclear import/export coefficient	p^{Mad}	0.015	μm/s
Effective diffusion coefficient of Mad and pMad	D	5	$\mu m^2/s$

"Standard" parameter set constrained by experimental data. The parameters are defined as follows: k_1 is the kinase activity constant; k_2 is the phosphatase activity constant; p_{in}^{pMad} is the nuclear envelope permeability to pMad import; p_{out}^{pMad} is the nuclear envelope permeability to pMad export; k_{on} is the rate constant of pMad binding to the nuclear matrix and DNA; K is the corresponding dissociation equilibrium constant; p^{Mad} is the nuclear envelope permeability to pMad import/export; and D is pMad diffusivity (see also Methods).

Loss of Dd Disrupts the Proper Differentiation of GSCs. Asymmetric stem cell division balances self-renewal and differentiation of a stem cell and is important for tissue homeostasis. Does loss of pMad asymmetry caused by loss of Dd have any impact on tissue homeostasis? The ddd^p/ddd^p germaria possessed a slightly increased number of pMad positive, GSC-like cells near the niche (3.3 ± 1.5 [$n = 27$] in control, 4.6 ± 1.2 [$n = 27$] in ddd^p/ddd^p, $P < 0.001$, Fig. 5 *A* and *B*), indicating that the Dd loss has a slight impact on the timing of GSC differentiation.

Expression of constitutively active Tkv in germ cells (*nosGal4 > tkvCA*) is often utilized to induce a tumorous germarium filled with undifferentiated germ cells (34). Although these tumor cells possessed round fusomes, a hallmark of undifferentiated cells, many of the tumor cells showed only weak pMad staining, resembling a preCB stage (Fig. 5 *C* and *E*). However, we found that introducing one *Dd* mutant allele ($ddd^p/+$) to the TkvCA background led to strong pMad throughout the tumor (Fig. 5*D*). Strong pMad combined with a round fusome indicates GSC identity. Moreover, this condition ($ddd^p/+$ and TkvCA) significantly increased the number of tumor cells (Fig. 5 *F* and *G*), possibly due to a cell fate switch from a preCB to an GSC-like state (Fig. 5*H*).

Taken together, our study shows that down-regulation of niche signaling, before a stem cell and its differentiating daughter cell, complete cytokinesis, plays an important role in ensuring that the differentiating daughter exits the stem cell state.

Discussion

During asymmetric stem cell division, two daughter cells acquire different cell fates. The *Drosophila* ovarian niche differentially activates an GSC and a preCB because of the distinct position of these cells, the former adjacent to the niche and the latter displaced from the niche. What is the initial cause of the difference? While many factors have been identified that can amplify and/or ensure the already existent niche signal difference, it has been unknown how Mad, the immediate downstream molecule of the niche ligand, is initially regulated during GSC division.

Mad is phosphorylated by active receptors at the side of GSC near the niche and then travels throughout the cytoplasm before entering the nucleus. The GSC–preCB pairs continue to share the cytoplasm for at least several hours after mitosis (20). Consistent with previous studies, we observed that Mad diffuses throughout the cytoplasm of the GSC and preCB. We found, however, that during this phase, the pMad levels in the nuclei of the GSC and preCB are already asymmetric (G1/S pMad asymmetry). We determined that local activation of the kinase at the niche-GSC contact site is not sufficient for G1/S pMad asymmetry. Moreover, neither increasing the activity of kinase nor compromising the rate of Mad degradation affected G1/S pMad asymmetry. We discovered that the Mad phosphatase, Dd, which dephosphorylates Mad at the nuclear pores in both GSC and preCB cells, is an essential factor in the formation of early asymmetric partitioning of pMad.

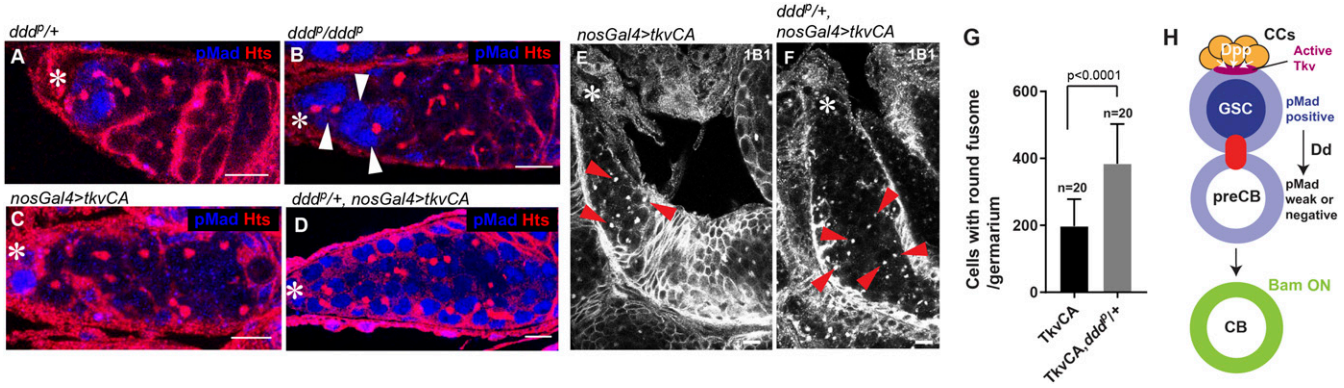

Fig. 5. Loss of Dd disrupts the proper differentiation of GSCs. (*A–D*) Hts (fusome and somatic cell membrane) and anti-pMad staining (blue) of germaria from indicated genotypes. (*B*) White arrows indicate extra pMad positive cells away from CCs. (*C* and *D*) anti-pMad staining of TkvCA expressing tumor cells without (*C*) or with (*D*) introduction of one copy of the ddd^p allele. (*E* and *F*) Representative images of Hts staining of tumor cells expressing TkvCA without (*E*) or with (*F*) one copy of the ddd^p allele. Red arrows in *E* and *F* show round fusomes, a hallmark of undifferentiated cells. (*G*) Comparison of GSC-like cell number (cells with round fusome) in TkvCA expressing germarium with or without one copy of the ddd^p allele. The *P* value was calculated by Student's *t* test. The 20 germaria were scored for each data point. (*H*) Model. The pMad asymmetry formation ensures GSC to preCB differentiation. Asterisks indicate the location of CCs. (Scale bar, 10 μm.)

To gain insight into the mechanisms responsible for the observed G1/S asymmetry, we formulated a mathematical model, which included all major factors governing the spatiotemporal dynamics of pMad, and constrained it by the experimental data obtained in this study. Our model suggests that a combination of the asymmetrically localized activated kinases, which reside at the site of contact between the GSC plasma membrane and the niche, together with sufficiently active phosphatase that is distributed symmetrically between nuclear envelopes of the GSC and preCB, is sufficient to explain the experimentally observed asymmetry of pMad levels in the GSC–preCB pairs.

Analysis of the model revealed that for pMad asymmetry to occur, it is necessary that the positive and negative regulators of pMad (the kinases and phosphatases) be separated in space, as this brings about spatial gradients of pMad. However, this condition is not sufficient, as the gradients could be shallow. The modeling showed, furthermore, that the steepness of pMad gradients is exclusively determined by the interplay of two factors: pMad dephosphorylation that steepens the gradients and pMad diffusion in the cytoplasm that levels them out. Active regulation of the pMad diffusivity, which is determined by protein size and effective viscosity of the cytoplasm (35), is unlikely. This makes the phosphatase activity an essential factor determining pMad asymmetry. To a lesser degree, the asymmetry also depends on the permeability of nuclear pores to pMad export from the nucleus, since the dephosphorylation of pMad occurs inside the nucleus.

In summary, our study identifies and explains a mechanism by which a stem cell can rapidly set up an initial asymmetry with respect to an extrinsic signal thus providing a conceptual framework for understanding the dynamics of niche-stem cell signaling.

Methods

Fly Husbandry and Strains. All fly stocks were raised in standard Bloomington medium at 25 °C. The following fly stocks were used, UASp-tkvCA (9) (gift from Michael Buszczak), Ubi-Pavarotti (Pav)-GFP (36) (gift from Yukiko Yamashita), hypomorphic *Dd* mutant (*ddd*^{o}) (gift from Shin Sugiyama) (23), FuA, a strong fu mutant allele with a deletion in the extracatalytic domain (gift from Jin Jiang) (37), UAS-Mad-MGM (gift from Edward Eivers) (24). The following stocks were obtained from the Bloomington stock center: w[1118]; P{w[+mC]=GAL4::VP16-nos.UTR}CG6325[MVD1](BDSC4937), w[*];P{w[+mC]=UASp-alphaTub84B.tdEOS}7M (BDSC51314);w[1118];P{w[+mC]=Ubi-GFP.E2f1.1–230}19P{w[+mC]=Ubi-mRFP1.CycB.1–266}12/CyO, P{ry[+t7.2]=en1}wg[en11]; MKRS/TM6B, Tb[1] (BDSC55098); for *Dd* RNAi, short hairpin RNA (y[1] v[1]; P{y[+t7.7] v[+t1.8]=TRiP.GL01268}attP2/TM3, Sb[1], BDSC41840) was expressed under the control of nosGal4 (see below for validation method). The control cross for RNAi was designed with matching gal4 and UAS copy number using TRiP background stocks, y[1] v[1]; P{y[+t7.7]=CaryP}attP40 (BDSC36304) or y[1] sc[*] v[1] sev[21]; P{y[+t7.7] v[+t1.8]=UAS-mCherry.VALIUM10}attP2 (BDSC35787) at 25 °C.

Immunofluorescent Staining. Ovaries were dissected from flies 3 d after eclosion in phosphate-buffered saline (PBS) and fixed in 4% formaldehyde in PBS for 30 to 60 min. For anti-Dd staining, ovaries were fixed in 4% formaldehyde in 90% ethanol at −20 °C for 10 min. Next, ovaries were permeabilized in PBS + 0.3% TritonX100 (PBST) for at least 30 min, followed by incubation with primary antibody in 3% bovine serum albumin (BSA) in PBST at 4 °C overnight. Samples were washed for 60 min (three times for 20 min each) in PBST, incubated with secondary antibody in 3% BSA in PBST at 4 °C overnight, and then washed for 60 min (three times for 20 min each) in PBST. Samples were then mounted using VECTASHIELD with DAPI. The primary antibodies used are in *SI Appendix*, Table S3. AlexaFluor-conjugated secondary antibodies were used at a dilution of 1:400. Images were taken using a Zeiss LSM800 confocal microscope with a 63× oil immersion objective (numerical aperture = 1.4) and processed using Zen software or Fiji.

Generation of pUASp-*Dd-VNm9*, pUASp-*medea-VNm9*, pUASp-*GFP-mad*, and pUASp-*VC-mad* Flies. See *SI Appendix, Supplemental Methods* and Table S3 for details.

Quantification of pMad Ratio. Ovaries were dissected from flies 3 d after eclosion and stained with anti-Hts (fusome marker) and anti-Vasa (germ cell cytoplasm marker) antibodies to determine the cell cycle stage of GSC–preCB pairs. From z stacks (0.5 μm interval), GSC–preCB pairs were manually identified. Measurements were performed in a single z section taken approximately at equator level of the cell. Mean intensity values for the pMad channel were determined from ∼2 × 2 μm^2 square regions of GSC or preCB nuclei or the cytoplasm for mitotic cells close to the apical or distal pole of the cell. Background signals were measured in the nuclei of differentiating germ cells then subtracted from each measurement. The pMad ratio was determined as asymmetric when preCB/GSC nuclear ratio was less than 0.8.

Live Imaging. Ovaries were dissected from flies 3 d after eclosion in 1 mL of prewarmed (25 °C) Schneider's *Drosophila* medium supplemented with 10% fetal bovine serum and glutamine–penicillin–streptomycin. Dissected ovaries were placed onto "Gold Seal Rite-On Micro Slides two-etched rings" with a drop of media, then covered with coverslips. An inverted Zeiss LSM800 confocal microscope with a 63× oil immersion objective (NA = 1.4) was used for imaging.

Photoconversion and Photobleaching. Photoconversion of αTub-tdEOS or photobleaching of GFP-Mad was accomplished using a Zeiss LSM800 confocal laser scanning microscope with a 63×/1.4 NA oil objective. Zen software was used for the programming of each experiment. Laser powers and iteration were optimized to achieve an ∼50 to 70% conversion or an ∼70 to 100% bleach. For the photoconversion, a 405-nm laser (14% laser power with no iteration) was used. For the photobleaching, a 488-nm laser (100% laser power with 15 iterations) was used. The distribution change of fluorescence was monitored every 10 s for the indicated duration.

See *SI Appendix, Supplemental Methods* for determination of cytoplasmic connectivity by αTub-tdEOS photoconversion or by GFP-Mad photobleaching.

The worksheet used to perform the least-square minimization and to identify connected cells is included in Dataset S1. The data used in Fig. 1*E* and *SI Appendix*, Fig. S8 are also given in Dataset S2. Movies of the photobleaching experiments are available in the BioStudies database (https://www.ebi.ac.uk/biostudies) under accession number S-BSST556.

Quantification of BiFC Dots on the Nuclear Surface. An GSC or a preCB expressing Dd-VNm9 and VC-Mad (*nosGal4* > *Dd-VNm9*, *VC-mad*) was used to take a z stack (0.4 μm interval) covering the entire area of the nuclear surface. A small region (2 × 2 μm^2 square region) within the apical half (near the CCs) or distal half of the nuclear surface was manually chosen for the measurement. The total number of dots appearing in each area was counted by using the Octane1.5.1 particle counting function (Superresolution Imaging and Single Molecule Tracking Software; https://github.com/jiyuuchc/Octane) and divided by the area (4 μm^2) used for counting. The cytoplasmic area in each cell was used to determine the background level.

Quantitative RT-PCR to Validate RNAi-Mediated Knockdown of Genes. Ovaries from 20 female progeny, age 3 to 7 d, were collected and homogenized in TRIzol Reagent (Invitrogen), and RNA was extracted following the manufacturer's instructions. One microgram of total RNA was reverse transcribed to complementary DNA using SuperScript III First-Strand Synthesis Super Mix (Invitrogen) with Oligo (dT)20 Primer. The qPCR was performed, in duplicate, using SYBR green Applied Biosystems Gene Expression Master Mix on a CFX96 Real-Time PCR Detection System (Bio-Rad). Relative quantification was performed using the comparative threshold cycle method. *Dd* transcript in *Dd* RNAi ovary (*nosGal4* > *Dd RNAi*) was 23.9% of the control level.

Mathematical Modeling.

Model geometry. Cells are defined by two intersecting identical spheres with an 8.3-μm diameter. Two nuclei are modeled by spheres with 5-μm diameters that are concentric with respective large spheres. Parameters of the model geometry are the averages of the respective sizes of measurements from experimental images (n = 15 for GSCs and n = 15 for preCBs).

Let Ω_{cyto}, Ω_{nucl1}, and Ω_{nucl2} denote the spaces occupied by the cytosol and nuclei of GSC and preCB, respectively, and (x, y, z) are the Cartesian coordinates of a spatial point. The nuclei Ω_{nucl1} and Ω_{nucl2} are then modeled as

$$\{\Omega_{nucl1} \,|\, (x^2 + (y - 4.5)^2 + z^2 \le 2.5^2)\} \quad \text{and} \quad \{\Omega_{nucl2} \,|\, (x^2 + (y - 12.5)^2 + z^2 \le 2.5^2)\},$$

and the overall space $\Omega = \Omega_{cyto} \cup \Omega_{nucl1} \cup \Omega_{nucl2}$ that includes the cytosol and

the nuclei is defined as $\{\Omega \mid (x^2+(y-4.5)^2+z^2 \le 4.15^2) \cup (x^2+(y-12.5)^2+z^2 \le 4.15^2)\}$.

Model parameters. The model approximates all processes as continuous and yields spatial distributions of Mad and pMad, both in the cytoplasm and nuclei. Rates of phosphorylation and dephosphorylation, as well as fluxes between the nuclei and cytoplasm, are assumed to be linear functions of respective concentrations, [*Mad*] and [*pMad*].

k_1 and k_2. Because enzymatic reactions occur at the membranes, their rates may also be regarded as flux densities of the corresponding volume variables. Specifically, the rate of phosphorylation is described as $k_1[Mad]_{cyto}$, where constant k_1 is the product of a phosphorylation rate constant and a surface density of the activated receptor. The units of k_1 are μm per second. Similarly, the rate of dephosphorylation is $k_2[pMad]_{nucl,i}$, with constant k_2 being the product of a dephosphorylation rate constant and the phosphatase surface density, assumed to be uniform over a nuclear envelope and the same for both envelopes, and index $i = 1,2$ denoting the nuclei of GSC ($i = 1$) and preCB ($i = 2$).

$p^{(p)Mad}$ and K. The accumulation of pMad in cell nuclei is due to unequal permeabilities of a nuclear envelope for pMad import/export (38, 39). In the model, we describe the net pMad influx density as $p_{in}^{pMad}[pMad]_{cyto} - p_{out}^{pMad}[pMad]_{nucl,i}$, where p_{in}^{pMad} and p_{out}^{pMad} are the respective permeabilities of a nuclear envelope and index i denotes the nuclei of GSC ($i = 1$) and CB ($i = 2$). Consistently with a published study (38), we assume $p_{in}^{pMad} > p_{out}^{pMad}$. The pMad binding to the nuclear matrix and DNA is approximated by a first-order reversible reaction with the rate $k_{on}([pMad]_{nucl,i} - K[pMad]_{nucl,i}^{bound})$, where k_{on} is the on-rate constant in s^{-1} and K is the dimensionless dissociation constant. While Mad is also partially bound in the nuclei, no accumulation of Mad is observed in the nuclei of nonactivated cells, likely because the effect of binding was counterbalanced by inequality of permeabilities in favor of export (38, 39). In our model, we thus ignore, for simplicity, the binding of Mad inside the nuclei and describe the net Mad influx density as $p^{Mad}([Mad]_{cyto} - [Mad]_{nucl,i})$.

The diffusion of Mad and pMad molecules, both in the cytoplasm and nuclei, is described by the same diffusion coefficient D.

Parameter values were constrained by the data in Figs. 1 *D* and *E* and 2*C* and by the experimentally measured GSC nucleus/cytoplasm ratio of pMad concentrations, 4.1 ± 1.2 ($n = 10$), and the nuclear GSC/preCB ratio of total Mad (both phosphorylated and unphosphorylated), 1.24 ± 0.11 ($n = 10$).

Equations. Let $\mathbf{r} \equiv \mathbf{r}(x,y,z)$ be the radius vector of a point (x,y,z) in Ω.

The governing equations in the cytosol ($\mathbf{r} \in \Omega_{cyto}$) are the following:

$$\partial_t[Mad]_{cyto} = D\nabla^2[Mad]_{cyto} \quad \textbf{[1.1]}$$

$$\partial_t[pMad]_{cyto} = D\nabla^2[pMad]_{cyto}. \quad \textbf{[1.2]}$$

Eq. **1** is subject to boundary conditions at the plasma membrane $\partial\Omega$ and nuclear envelopes $\partial\Omega_{nucl1}$ and $\partial\Omega_{nucl2}$. At the plasma membrane, the boundary condition for Eq. **1.1** is nonzero only for $\mathbf{r} \in (\partial\Omega \cap y \le 1)$, the points comprising the red "cap" in Fig. 4*B*,

$$-D\nabla[Mad]_{cyto} \cdot \mathbf{n}|_{\mathbf{r}\in\partial\Omega} = k_1[Mad]_{cyto}|_{\mathbf{r}\in(\partial\Omega\cap y\le 1)},$$

where $\mathbf{n}$ is the outward normal at $\partial\Omega$.

At the nuclear envelopes, the boundary conditions for [*Mad*] are the following:

$$\begin{aligned} -D\nabla[Mad]_{cyto} \cdot \mathbf{n}|_{\mathbf{r}\in\partial\Omega_{nucl1}} &= p^{Mad}\left([Mad]_{cyto} - [Mad]_{nucl1}\right)|_{\mathbf{r}\in\partial\Omega_{nucl1}} \\ -D\nabla[Mad]_{cyto} \cdot \mathbf{n}|_{\mathbf{r}\in\partial\Omega_{nucl2}} &= p^{Mad}\left([Mad]_{cyto} - [Mad]_{nucl2}\right)|_{\mathbf{r}\in\partial\Omega_{nucl2}} \end{aligned},$$

where vectors $\mathbf{n}$ are the outward, with respect to Ω_{cyto}, normals at $\partial\Omega_{nucl1}$, and $\partial\Omega_{nucl2}$, respectively (i.e., the normals are directed toward the interior of the nuclei).

Similarly, the boundary conditions for Eq. **1.2** are as follows:

$$-D\nabla[pMad]_{cyto} \cdot \mathbf{n}|_{\mathbf{r}\in\partial\Omega} = -k_1[Mad]_{cyto}|_{\mathbf{r}\in(\partial\Omega\cap y\le 1)},$$

where $\mathbf{n}$ is the outward normal vector at $\partial\Omega$, and

$$\begin{aligned} -D\nabla[pMad_{cyto}] \cdot \mathbf{n}|_{\mathbf{r}\in\partial\Omega_{nucl1}} &= \left(p_{in}^{pMad}[pMad]_{cyto} - p_{out}^{pMad}[pMad]_{nucl1}\right)|_{\mathbf{r}\in\partial\Omega_{nucl1}} \\ -D\nabla[pMad_{cyto}] \cdot \mathbf{n}|_{\mathbf{r}\in\partial\Omega_{nucl2}} &= \left(p_{in}^{pMad}[pMad]_{cyto} - p_{out}^{pMad}[pMad]_{nucl2}\right)|_{\mathbf{r}\in\partial\Omega_{nucl2}} \end{aligned},$$

where vectors $\mathbf{n}$ are the outward, with respect to Ω_{cyto}, normals to $\partial\Omega_{nucl1}$, and $\partial\Omega_{nucl2}$, respectively.

The equations in the nuclei [$\mathbf{r} \in (\Omega_{nucl,1} \cup \Omega_{nucl,2})$] are the following:

$$\partial_t[Mad]_{nucl,i} = D\nabla^2[Mad]_{nucl,i}, \ (i = 1,2) \quad \textbf{[2.1]}$$

$$\begin{aligned} \partial_t[pMad]_{nucl,i} &= D\nabla^2[pMad]_{nucl,i} \\ &\quad - k_{on}\left([pMad]_{nucl,i} - K[pMad]_{nucl,i}^{bound}\right), \ (i = 1,2) \end{aligned} \quad \textbf{[2.2]}$$

and the equation governing $[pMad]_{nucl,i}^{bound}$ is $\partial_t[pMad]_{nucl,i}^{bound} = k_{on}([pMad]_{nucl,i} - K[pMad]_{nucl,i}^{bound})$.

Eq. **2** is subject to boundary conditions at the nuclear envelopes $\partial\Omega_{nucl1}$ and $\partial\Omega_{nucl2}$. The boundary conditions for Eq. **2.1** are as follows:

$$\begin{aligned} -D\nabla[Mad]_{nucl,1} \cdot \mathbf{n}|_{\mathbf{r}\in\partial\Omega_{nucl1}} &= \left(p^{Mad}\left([Mad]_{cyto} - [Mad]_{nucl,1}\right)\right. \\ &\quad \left. + k_2[pMad]_{nucl,1}\right)|_{\mathbf{r}\in\partial\Omega_{nucl1}}, \\ -D\nabla[Mad]_{nucl,2} \cdot \mathbf{n}|_{\mathbf{r}\in\partial\Omega_{nucl2}} &= \left(p^{Mad}\left([Mad]_{cyto} - [Mad]_{nucl,2}\right)\right. \\ &\quad \left. + k_2[pMad]_{nucl,2}\right)|_{\mathbf{r}\in\partial\Omega_{nucl2}}, \end{aligned}$$

where $\mathbf{n}$ are the respective normal vectors at $\partial\Omega_{nucl1}$ and $\partial\Omega_{nucl2}$, outward with respect to Ω_{cyto} (i.e., the normals are directed toward the interior of the nuclei).

Similarly, the boundary conditions for Eq. **2.2** are as follows:

$$\begin{aligned} -D\nabla[pMad_{nucl1}] \cdot \mathbf{n}|_{\mathbf{r}\in\partial\Omega_{nucl1}} &= \left(\left(p_{in}^{pMad}[pMad]_{cyto} - p_{out}^{pMad}[pMad]_{nucl1}\right)\right. \\ &\quad \left. - k_2[pMad]_{nucl1}\right)|_{\mathbf{r}\in\partial\Omega_{nucl1}}, \\ -D\nabla[pMad_{nucl2}] \cdot \mathbf{n}|_{\mathbf{r}\in\partial\Omega_{nucl2}} &= \left(\left(p_{in}^{pMad}[pMad]_{cyto} - p_{out}^{pMad}[pMad]_{nucl2}\right)\right. \\ &\quad \left. - k_2[pMad]_{nucl2}\right)|_{\mathbf{r}\in\partial\Omega_{nucl2}}, \end{aligned}$$

using the same definition of vectors $\mathbf{n}$ as above.

The system of Eqs. 1 and **2** is initialized as follows: for all $\mathbf{r} \in \Omega$, $[Mad](\mathbf{r}, 0) = 1$ a. u. (an arbitrary unit of volume density) and $[pMad](\mathbf{r}, 0) = 0$.

The mathematical model outlined above was solved numerically with Virtual Cell (VCell), a publicly available software for computational modeling in cell biology (40, 41). Simulations were run with a VCell fully implicit spatial solver using a uniform orthogonal mesh with a mesh size of 0.2 μm. The steady-state solutions were obtained by running simulations for sufficiently long end times (typically, the end time of 10^3 s was sufficient to reach a steady state, with the exception of smaller values of p^{Mad} and k_2 that, respectively, required the end times of $2 \cdot 10^3$ and $3 \cdot 10^3$ s).

The VCell implementation of the model can be found in the VCell database of public MathModels under username "boris"; the model name is "Inaba_Model_public_final." Note that in this implementation, the units of concentration are μM (1 μM = 602 molecules per μm^3).

Statistical Analysis and Graphing. No statistical methods were used to predetermine sample size. The experiment values were not randomized. The investigators were not blinded to allocation during experiments and outcome assessment. Statistical analysis and graphing were performed using GraphPad prism 7 software. Data are shown as means ± SD. The *P* values from Student's *t* test or adjusted *P* values from Dunnett's multiple comparisons test are provided. Z test was used for determination of cell connectivity, described in *SI Appendix*, Fig. S1.

Data Availability. Time lapse imaging files (CZI. TIF.) data have been deposited in the BioStudies database (https://www.ebi.ac.uk/biostudies) (S-BSST556). All other study data are included in the article and/or supporting information.

ACKNOWLEDGMENTS. We thank Yukiko Yamashita, Michael Buszczak, Yasushi Saka, Edward Eivers, Shin Sugiyama, the Bloomington *Drosophila* Stock Center, and the Developmental Studies Hybridoma Bank for reagents; Laurinda Jaffe and Mark Terasaki for discussion; Christopher Bonin for manuscript editing; and Guy Myette for fly stock maintenance. B.M.S. thanks

Leslie Loew for his continued support. This research is supported by Maximizing Investigators' Research Award (MIRA) (R35), 1R35GM128678-01 from National Institutes of Health (NIH), National Institute for General Medical Sciences (NIGMS) and start-up funds from UConn Health to M.I., and by a grant, P41 GM103313 from NIH, NIGMS. VCell is currently supported by a grant, R24 GM137787 from NIH, NIGMS.

1. A. Spradling, M. T. Fuller, R. E. Braun, S. Yoshida, Germline stem cells. *Cold Spring Harb. Perspect. Biol.* **3**, a002642 (2011).
2. T. Xie, A. C. Spradling, Decapentaplegic is essential for the maintenance and division of germline stem cells in the *Drosophila* ovary. *Cell* **94**, 251–260 (1998).
3. X. Song *et al*., Bmp signals from niche cells directly repress transcription of a differentiation-promoting gene, bag of marbles, in germline stem cells in the *Drosophila* ovary. *Development* **131**, 1353–1364 (2004).
4. D. Chen, D. McKearin, Dpp signaling silences bam transcription directly to establish asymmetric divisions of germline stem cells. *Curr. Biol.* **13**, 1786–1791 (2003).
5. D. Chen, D. M. McKearin, A discrete transcriptional silencer in the bam gene determines asymmetric division of the Drosophila germline stem cell. *Development* **130**, 1159–1170 (2003).
6. L. Xia *et al*., The niche-dependent feedback loop generates a BMP activity gradient to determine the germline stem cell fate. *Curr. Biol.* **22**, 515–521 (2012).
7. X. Wang, R. E. Harris, L. J. Bayston, H. L. Ashe, Type IV collagens regulate BMP signalling in *Drosophila*. *Nature* **455**, 72–77 (2008).
8. V. Van De Bor *et al*., Companion blood cells control ovarian stem cell niche microenvironment and homeostasis. *Cell Rep.* **13**, 546–560 (2015).
9. Z. Guo, Z. Wang, The glypican Dally is required in the niche for the maintenance of germline stem cells and short-range BMP signaling in the *Drosophila* ovary. *Development* **136**, 3627–3635 (2009).
10. R. E. Harris, M. Pargett, C. Sutcliffe, D. Umulis, H. L. Ashe, Brat promotes stem cell differentiation via control of a bistable switch that restricts BMP signaling. *Dev. Cell* **20**, 72–83 (2011).
11. M. Liu, T. M. Lim, Y. Cai, The *Drosophila* female germline stem cell lineage acts to spatially restrict DPP function within the niche. *Sci. Signal.* **3**, ra57 (2010).
12. C. Schulz, C. G. Wood, D. L. Jones, S. I. Tazuke, M. T. Fuller, Signaling from germ cells mediated by the rhomboid homolog stet organizes encapsulation by somatic support cells. *Development* **129**, 4523–4534 (2002).
13. L. Xia *et al*., The Fused/Smurf complex controls the fate of *Drosophila* germline stem cells by generating a gradient BMP response. *Cell* **143**, 978–990 (2010).
14. X. Jiang *et al*., Otefin, a nuclear membrane protein, determines the fate of germline stem cells in Drosophila via interaction with Smad complexes. *Dev. Cell* **14**, 494–506 (2008).
15. C.-Y. Tseng *et al*., Smad-independent BMP signaling in somatic cells limits the size of the germline stem cell pool. *Stem Cell Reports* **11**, 811–827 (2018).
16. S. Eliazer *et al*., Lsd1 restricts the number of germline stem cells by regulating multiple targets in escort cells. *PLoS Genet.* **10**, e1004200 (2014).
17. M. de Cuevas, A. C. Spradling, Morphogenesis of the *Drosophila* fusome and its implications for oocyte specification. *Development* **125**, 2781–2789 (1998).
18. J. Mathieu *et al*., Aurora B and cyclin B have opposite effects on the timing of cytokinesis abscission in *Drosophila* germ cells and in vertebrate somatic cells. *Dev. Cell* **26**, 250–265 (2013).
19. E. T. Ables, D. Drummond-Barbosa, Cyclin E controls *Drosophila* female germline stem cell maintenance independently of its role in proliferation by modulating responsiveness to niche signals. *Development* **140**, 530–540 (2013).
20. N. R. Matias, J. Mathieu, J.-R. Huynh, Abscission is regulated by the ESCRT-III protein shrub in *Drosophila* germline stem cells. *PLoS Genet.* **11**, e1004653 (2015).
21. H. Urrutia, A. Aleman, E. Eivers, *Drosophila* Dullard functions as a Mad phosphatase to terminate BMP signaling. *Sci. Rep.* **6**, 32269 (2016).
22. T. D. Hinnant, A. A. Alvarez, E. T. Ables, Temporal remodeling of the cell cycle accompanies differentiation in the *Drosophila* germline. *Dev. Biol.* **429**, 118–131 (2017).
23. Z. Liu *et al*., Negative modulation of bone morphogenetic protein signaling by Dullard during wing vein formation in *Drosophila*. *Dev. Growth Differ.* **53**, 822–841 (2011).
24. E. Eivers *et al*., Mad is required for wingless signaling in wing development and segment patterning in *Drosophila*. *PLoS One* **4**, e6543 (2009).
25. C.-D. Hu, Y. Chinenov, T. K. Kerppola, Visualization of interactions among bZIP and Rel family proteins in living cells using bimolecular fluorescence complementation. *Mol. Cell* **9**, 789–798 (2002).
26. Y. Saka, A. I. Hagemann, O. Piepenburg, J. C. Smith, Nuclear accumulation of Smad complexes occurs only after the midblastula transition in Xenopus. *Development* **134**, 4209–4218 (2007).
27. Y. Kim *et al*., A conserved phosphatase cascade that regulates nuclear membrane biogenesis. *Proc. Natl. Acad. Sci. U.S.A.* **104**, 6596–6601 (2007).
28. N. Zielke *et al*., Fly-FUCCI: A versatile tool for studying cell proliferation in complex tissues. *Cell Rep.* **7**, 588–598 (2014).
29. S. G. Wilcockson, H. L. Ashe, *Drosophila* ovarian germline stem cell cytocensor projections dynamically receive and attenuate BMP signaling. *Dev. Cell* **50**, 296–312.e5 (2019).
30. L Luo, H. Wang, C. Fan, S. Liu, Y. Cai, Wnt ligands regulate Tkv expression to constrain Dpp activity in the Drosophila ovarian stem cell niche. *J. Cell Biol.* **209**, 595–608 (2015).
31. T. Akiyama *et al*., Dally regulates Dpp morphogen gradient formation by stabilizing Dpp on the cell surface. *Dev. Biol.* **313**, 408–419 (2008).
32. S. Y. Shvartsman, R. E. Baker, Mathematical models of morphogen gradients and their effects on gene expression. *Wiley Interdiscip. Rev. Dev. Biol.* **1**, 715–730 (2012).
33. B. N. Kholodenko, Spatially distributed cell signalling. *FEBS Lett.* **583**, 4006–4012 (2009).
34. M. O. Casanueva, E. L. Ferguson, Germline stem cell number in the *Drosophila* ovary is regulated by redundant mechanisms that control Dpp signaling. *Development* **131**, 1881–1890 (2004).
35. H. C. Berg, *Random Walks in Biology* (Princeton University Press, 1993), pp. 152.
36. G. Minestrini, E. Máthé, D. M. Glover, Domains of the pavarotti kinesin-like protein that direct its subcellular distribution: Effects of mislocalisation on the tubulin and actin cytoskeleton during *Drosophila* oogenesis. *J. Cell Sci.* **115**, 725–736 (2002).
37. G. Alves *et al*., Modulation of hedgehog target gene expression by the fused serine-threonine kinase in wing imaginal discs. *Mech. Dev.* **78**, 17–31 (1998).
38. Y. Li, W. Luo, W. Yang, Nuclear transport and accumulation of Smad proteins studied by single-molecule microscopy. *Biophys. J.* **114**, 2243–2251 (2018).
39. B. Schmierer, A. L. Tournier, P. A. Bates, C. S. Hill, Mathematical modeling identifies Smad nucleocytoplasmic shuttling as a dynamic signal-interpreting system. *Proc. Natl. Acad. Sci. U.S.A.* **105**, 6608–6613 (2008).
40. B. M. Slepchenko, L. M. Loew, Use of Virtual Cell in Studies of Cellular Dynamics. *International Review of Cell and Molecular Biology*, 1–56 (2010).
41. D. C. Resasco *et al*., Virtual Cell: computational tools for modeling in cell biology. *Wiley Interdiscip. Rev. Syst. Biol. Med.* **4**, 129–140 (2012).